# UNIVERSITY *of York*

This is a repository copy of *Shaped liquid drops generate MeV temperature electron beams with millijoule class laser*.

White Rose Research Online URL for this paper:
https://eprints.whiterose.ac.uk/210796/

Version: Published Version

## Article:

White Rose
university consortium
Universities of Leeds, Sheffield & York

eprints@whiterose.ac.uk
https://eprints.whiterose.ac.uk/

# Shaped liquid drops generate MeV temperature electron beams with millijoule class laser

Check for updates

Angana Mondal[1,2], Ratul Sabui[2], Sheroy Tata[1], R. M. G. M. Trines [3], S. V. Rahul [2], Feiyu Li[4,8], Soubhik Sarkar[1], William Trickey[5,9], Rakesh Y. Kumar[2], Debobrata Rajak [2], John Pasley [6], Zhengming Sheng[4,7], Jagannath Jha[1], M. Anand[2], Ram Gopal[2], A. P. L. Robinson[3] & M. Krishnamurthy [1,2] ✉

MeV temperature electrons are typically generated at laser intensities of $10^{18}$ W cm$^{-2}$. Their generation at non-relativistic intensities (~$10^{16}$ W cm$^{-2}$) with high repetition rate lasers is cardinal for the realization of compact, ultra-fast electron sources. Here we report a technique of dynamic target structuring of micro-droplets using a 1 kHz, 25 fs, millijoule class laser, that uses two collinear laser pulses; the first to create a concave surface in the liquid drop and the second, to dynamically-drive electrostatic plasma waves that accelerate electrons to MeV energies. The acceleration mechanism, identified as two plasmon decay instability, is shown to generate two beams of electrons with hot electron temperature components of 200 keV and 1 MeV, respectively, at an intensity of $4 \times 10^{16}$ Wcm$^{-2}$, only. The electron beams are demonstrated to be ideal for single shot high resolution (tens of $\mu m$) electron radiography.

Relativistic temperature electrons[1–7] higher than 0.5 MeV are generated typically with laser intensities of about $10^{18}$ W cm$^{-2}$. In gas targets one of the most successful methods of high-energy electron generation is laser wake-field acceleration (LWFA)[8]. However, at moderate intensities of $10^{17}$ W cm$^{-2}$, LWFA becomes inefficient since the acceleration gradient formed is only about a few GV/m[9]. Nonetheless, LWFA, using mJ-class table-top, high-repetition (≥0.5 kHz) laser systems, have been demonstrated[10,11]. For example, a quasi-monoenergetic electron beam of 100 keV was observed in interaction of tightly focused 800 nm, 10 mJ, 32 fs pulses reaching an intensity of $3 \times 10^{18}$ W cm$^{-2}$ with 100 $\mu m$ gas target[10]. Further, electron acceleration up to 1.5 MeV have also been observed in both He and $H_2$ gas jet interaction with 800 nm, 30 fs laser pulses focussed to a 9 $\mu m$ full-width at half maxima (FWHM) of pulse energy and 10 mJ[11]. New strategies, capable of exploiting different aspects of laser-plasma interaction, are necessary for reducing the required intensity to non-relativistic regimes ($10^{16}$ W cm$^{-2}$) for the realization of compact, high-repetition rate, ultrashort electron sources. Among various efforts, a noteworthy approach towards generating relativistic electrons with low laser intensities has been target modification. Although these experiments have been performed for many years[12–19] none have efficiently achieved relativistic electrons using moderate-intensity table-top lasers. Other experiments in the non-relativistic regime implement parametric processes like two-plasmon decay (TPD) initiated in long pulse (≥ps) laser interaction[20–22], which require high energy (100 mJ) laser pulses to reach even intensities of $10^{15}$–$10^{16}$ W cm$^{-2}$.

We report here, a technique of dynamic target structuring of micro-droplets, capable of generating 200 keV and 1 MeV electron temperatures at 1/100th of the intensity required by ponderomotive scaling ($10^{18}$ W cm$^{-2}$) to generate relativistic electron temperature. Combining the concepts of pre-plasma tailoring, optimized scale length and micro-optics, this method achieves two-plasmon decay boosted electron acceleration with ultrashort (25 fs) pulses at $4 \times 10^{16}$ W cm$^{-2}$, only. TPD is ideally observed for laser pulses with large pulse duration capable of generating long scale-length pre-plasma in which the plasma waves that accelerate the electrons are initiated[20–22]. For ultrashort pulses (25–40 fs), which generate steep electron density profiles, TPD is not efficient for electron acceleration with resulting $T_{hot}$ reaching only ~150 keV for intensities as high as $10^{18}$ W cm$^{-2}$ [23]. Therefore, the present experimental laser-pulse parameters are

[1]Tata Institute of Fundamental Research, Mumbai, India. [2]Tata Institute of Fundamental Research, Hyderabad, India. [3]Central Laser Facility, Rutherford Appleton Laboratory, Didcot, UK. [4]Department of Physics, University of Strathclyde, Glasgow, UK. [5]York Plasma Institute, Department of Physics, University of York, York, UK. [6]York Plasma Institute, School of Physics, Engineering and Technology, University of York, York, UK. [7]Laboratory for Laser Plasmas and School of Physics and Astronomy, Shanghai Jiao Tong University, Shanghai, China. [8]Present address: New Mexico Consortium, Los Alamos, NM 87544, US. [9]Present address: Laboratory for Laser Energetics, University of Rochester, Rochester, NY 14623, US. . ✉e-mail: mkrism@tifr.res.in

conventionally "non-ideal" for electron acceleration through TPD. With shot repeatability at kHz, this precise in-situ targetry produces directed, imaging quality beam-like electron emission beyond 4 MeV with millijoule class lasers, that can be transformational for time-resolved, microscopic studies in various fields of science[24–28].

## Results

Our method uses the classic parametric instabilities route executed on dynamically structured, size-limited droplet target. TPD is a parametric process when electromagnetic fields of $\omega_0$ frequency, generate two-plasmon waves of $\omega_0/2$ frequency in non-collinear direction. This process is based on three aspects: (i) dynamically shaped critical density surface of optimal length and concavity, (ii) appropriate plasma density gradient about the concave critical density surface and a (iii) mesoscopic liquid droplet target suspended in vacuum that is used to generate features (i) and (ii). A collinear pre-pulse sets up hydrodynamic heating and expansion of the convex liquid surface to create a concave surface. A dynamically cavitated concave liquid drop structure is shown to be formed both from experimental shadowgrams and hydrodynamic simulations. The main pulse incident at the apex of the concave surface generate a concave critical density surface. Evaporating liquid provides the low-density background, which is ionized by the focused laser pulse at $10^{14}$ W cm$^{-2}$ providing a plasma density gradient for the generation of plasma waves. As explained above, conventionally, femtosecond (~25 fs) pulses with steeper electron density profile are not optimal to take advantage of instability effects. However, these effects are invoked in the current experiments with millijoule (mJ), ≤100 fs laser pulses through oblique-incidence TPD induced by the in-situ target structuring, to achieve unprecedented hot electron temperatures at sub-relativistic intensities and kHz repetition rates. The unique geometry provides longer effective density scale lengths at oblique incidence, reducing the instability threshold for TPD[29–31] for the main pump laser beam which has an intensity of $4 \times 10^{16}$ W cm$^{-2}$ resulting in $T_{hot}$ components of 200 keV and 1 MeV. The 200 keV $T_{hot}$ component is measured to scale as $I^{4.5}$ in this laser intensity regime. The signature of the TPD is seen via Stimulated Raman scattered signal (SRS) that is formed at $3\omega_0/2$[20,32,33], $\omega_0$ is the laser frequency. The two directed electron beams generated simultaneously, a further proof of the TPD instability, whose direction is controlled by laser polarization, are shown to have fluxes bright enough to produce high resolution (14 μm) resolution electron radiograph, at 100 times lower intensity than relativistic intensity sources[25].

The present report describes the underlying mechanisms, corroborating experiments, together with 2D particle in-cell (PIC) simulations using the PIC codes SMILEI and EPOCH[34,35] and the radiation-hydrodynamic code h2d. The results presented in the main text are performed using EPOCH, while supplementary data consists of simulation results from both EPOCH and SMILEI. There are no technical reasons to use the two PIC codes or consistency issues between the two but this is purely owing to the operational convenience of the authors. Results from both codes are in good agreement, as shown in Supplementary Figs. 1 and 2 and Supplementary Note 1. Radiography applications are presented to demonstrate the viability of compact, low-emittance, short-burst sources for microscopy[28,36–38]. Since the target delivery is already set-up to operate at 1 MHz, it is reasonable to project scalability of this technique to the currently available high-repetition rate (~10 kHz) laser systems.

### Experimental results

A schematic, of the experimental set-up is shown in Fig. 1a. A detailed description of the detection methods is presented in the Methods section. In brief, the experiments are performed using a 2 mJ, 800 nm, 1 kHz Ti-Sapphire laser system generating 25 fs pulses. The corresponding on-target intensity being $4 \times 10^{16}$ W cm$^{-2}$, when focused to a beam waist of 11 μm. The target droplets are produced by fragmenting a 10 μm, pressurized (20 bar) Methanol jet, to a 1 MHz stream of equally separated 15 μm droplets with a piezoelectric vibrator. The experiments are performed at a pressure of $5 \times 10^{-1}$ mbar. Prior to the main laser-pulse interaction, dynamical structures, vital for the relativistic electrons, are generated by focusing a collinear pre-pulse on to the target droplet. The pre-pulse, containing only 5% of the main pulse energy and arriving 4 ns ahead, is identical in all other aspects to the main pulse. The incident laser polarization is fixed with a half-wave plate. The overlap of the droplet and the laser pulses, is monitored by visualization and measurement of the transmitted beam and maximization of the electron energy. Emerging electrons are detected using a magnetic field (0.11 T) bending electron spectrometer (ESM) with LANEX or image plate (IP) placed at 45° with respect to the incident laser beam.

Standard laser-plasma mechanisms predict that a spherical dielectric target of size about 20 times the wavelength and a focal spot size smaller than the target, should be akin to a macroscopic target, possibly with small local field enhancements caused by near field scattering at the spherical interface[7,39]. On interaction with a 25 fs pulse, such a system is expected to generate an electron temperature of about $11 \pm 0.6$ keV (Fig. 1b curve for 2D



**Fig. 1 | Experimental schematic and observations. a** Schematic of hot electron generation set-up from laser-Methanol droplet interaction at kHz rate with 800 nm, 2 mJ, 25 fs at $4 \times 10^{16}$ W cm$^{-2}$. Electron and X-ray spectrum measurements are performed using a magnetic field (0.11 T) bending electron spectrometer (ESM) with LANEX or image plate (IP) as detectors placed at 45° with respect to the backward laser propagation direction and a NaI(Tl) detector, respectively. **b** Comparison of experimental electron spectrum and temperature with those obtained from 2D particle-in-cell (PIC) code EPOCH for a spherical drop (black circles). The spectrum has been normalized to electron yield at 200 keV. **c** Electron spectrum measurement for 900 s with a high dynamic range detector (IP), showing relativistic temperature components larger than 1 MeV. The LANEX spectrum from **b** is superimposed (as magenta circles) on the image plate spectrum (blue circles) to highlight the 200 keV temperature component and the dynamic range of the LANEX detector. The error (standard deviation of each data point) in experimental data lies within the diameter of the representative symbols.
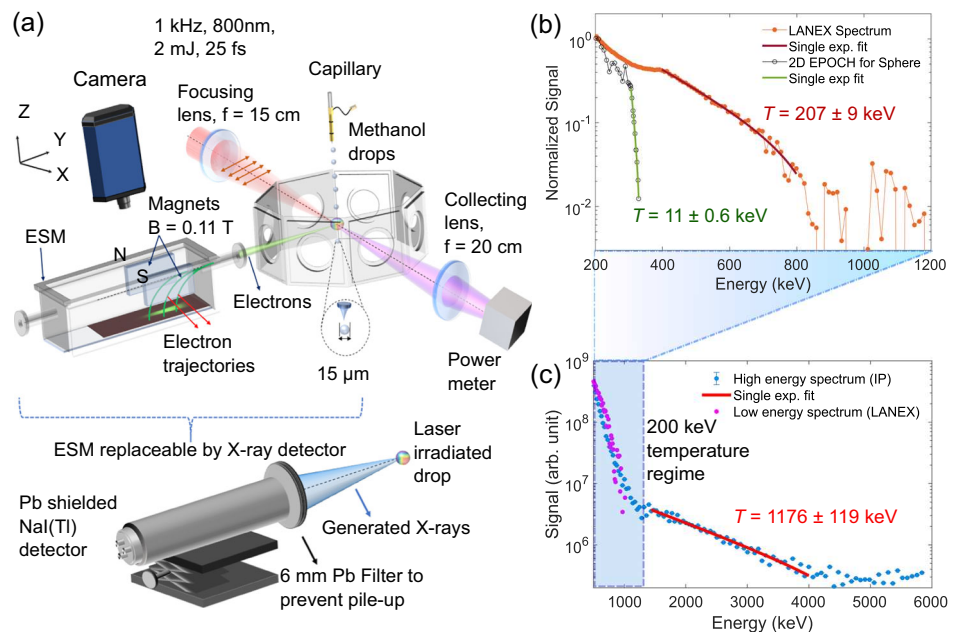
PIC with EPOCH) at $\sim 8.5 \times 10^{16}$ W cm$^{-2}$ intensity. Figure 1b shows a comparison of the electron spectrum obtained from 2D PIC for a spherical target with the experimentally obtained electron spectrum. The simulation parameters are elaborated in numerical modeling section. For the simple spherical target interaction, the high energy electron yield is seen to fall-off rapidly beyond 300 keV, with a sharp cut-off at about 400 keV. In contrast, our experimental measurements, obtained by electron spectrometry, show a dominant ~200 keV temperature measurable on a shot-to-shot basis (though ~8 s of data acquisition is presented for better statistics) using LANEX detectors (Fig. 1b) and a ~1.2 MeV electron temperature component extending beyond 4 MeV (Fig. 1c). Due to their weaker yield (few percent of 200 keV component), the 1 MeV component is captured in only long-time acquisition with the IP detectors that have $10^5$ orders signal detection range as opposed to that of $10^2$ in LANEX. The observed electron temperatures are also verified with bremsstrahlung X-ray measurements presented in Supplementary Fig. 3a and Supplementary Note 2.

To decipher the underlying mechanism, the angular distribution and the polarization dependence of the emitted electrons are measured. Figure 2, shows the electron emission to be confined in the laser polarization plane and oriented along two backward-directed cones at angles of $\sim \pm 50°$ with respect to the incident laser. Since, there is negligible backward and forward directed electrons (Supplementary Fig. 3c and Supplementary Note 2), Fig. 2a, d, e measurements have be performed with the image plates (IP) extending from the azimuthal angle of 20° to 120° on either side of the droplet, where the incident polarization is rotated first to 40° (Fig. 2b) and then to -40° with respect to the incidence plane (Fig. 2c). The directed emission of electrons at the aforementioned angles should not be mistaken as resonance absorption (RA) in spherical targets[39,40], since the obtained $T_{hot}$ and its intensity dependence, as shown in Fig. 3a, is ~10 and 13 times larger than would be expected from ponderomotive acceleration and RA[7,39], respectively. In addition, unlike in RA, the electron angular distribution is also highly tunable with the change in laser intensity, as shown in Fig. 3b.

Investigation of the laser-pulse parameters reveals that the uncharacteristically high $T_{hot}$ is attained only in the presence of a weak pre-pulse 4 ns ahead of the main pulse. A collinear two pulse experiment is set-up, to systematically change the pre-pulse intensity and determine the optimum

pre-pulse strength for maximum X-ray/electron generation. A clean laser beam (with no-pre-pulse) is split into two beams with a beam splitter: a pre-pulse with 10% energy and a delayed main pulse. Then intensity and polarization of the pre-pulse is controlled using a combination of a polariser and a half-wave plate while the time difference between the pre-pulse and the main pulse is varied using a delay-stage. The two beams are later combined by another beam splitter to maintain the collinear geometry. The details of the pre-pulse dependent measurement set-up and the photo-diode signals indicating the absence and presence of pre-pulse is presented in Supplementary Fig. 4 and Supplementary Note 3. Figure 3c shows the variation in X-ray yield as a function of pre-pulse percentage (in terms of the ratio of pre-pulse energy to the main pulse energy), for a main pulse of energy 1 mJ incident 4 ns after the pre-pulse. It is observed that the X-ray emission is negligible in the absence of any pre-pulse but rises sharply and saturates when the pre-pulse energy reaches about 4–5% of the main pulse energy. For all other results, we therefore use a pre-pulse containing 5% of the main pulse intensity. The incident pre-pulse is expected to increase main pulse absorption through pre-plasma generation[17,18,41]. However, using 2D PIC simulations with varying pre-plasma and laser conditions, shown in Supplementary Fig. 5 and Supplementary Note 4, it is observed that the presence of the pre-plasma alone, fails to generate relativistic electron temperatures in the $10^{16}$ W cm$^{-2}$ intensity regime. Systematic variation of the peak plasma density and laser intensity show that even at a higher laser intensity of about $\sim 1.5 \times 10^{17}$ W cm$^{-2}$, the electron energies are at least ten times smaller than the current experimental observations.

However in a micro-spherical target, a pre-pulse (25 fs pulse replica) does more than pre-plasma generation. A pre-pulse of 5% the intensity of the main pulse, appropriately timed, can cause significant modification of the structure of the droplet prior to the arrival of the main pulse. To visualize the pre-pulse effect on the droplet structure, a shadowgraphy measurement is implemented. Similar to the pre-pulse dependent studies, the laser pulse is split into two beams in a 8:92 ratio. The weaker beam, with an intensity comparable to the original pre-pulse, is used to simulate the pre-pulse effects on the droplet. The stronger beam is frequency doubled and used to image the transverse profile of the drop. The shadowgraphy image captured using a gated 12 bit CCD camera coupled with a 400 nm bandpass filter to reject



**Fig. 2 | Electron angular distribution as a function of laser polarization. a** Angular distribution when the laser polarization is rotated 40° to the plane of incidence. **b** Schematic showing the direction of incident laser polarization of 40° with respect to the plane of incidence (also marked with the half-wave plate (HWP) axis) and the subsequent orientation of the electron emission plane(green rectangle). **c** Schematic indicating the orientation of the electron emission plane(green rectangle) when the incident electric field rotated in the opposite direction (−40°) with respect to the plane of incidence. **d** Angular distribution when the laser polarization is −40° to the plane of incidence. **e** Reference angular distribution of electrons for the laser polarization in the plane of incidence.
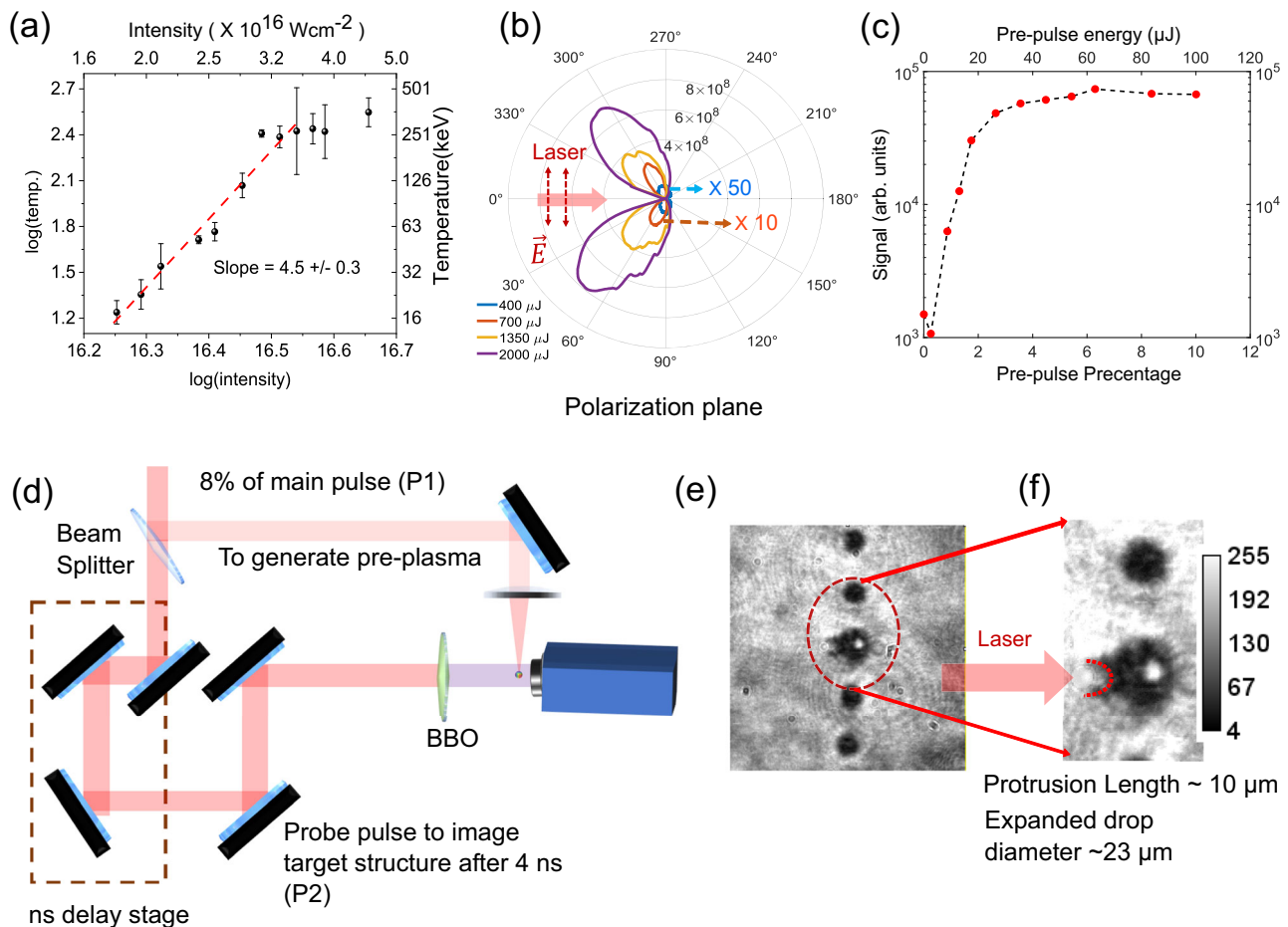
Protrusion Length ~ 10 μm
Expanded drop
diameter ~23 μm
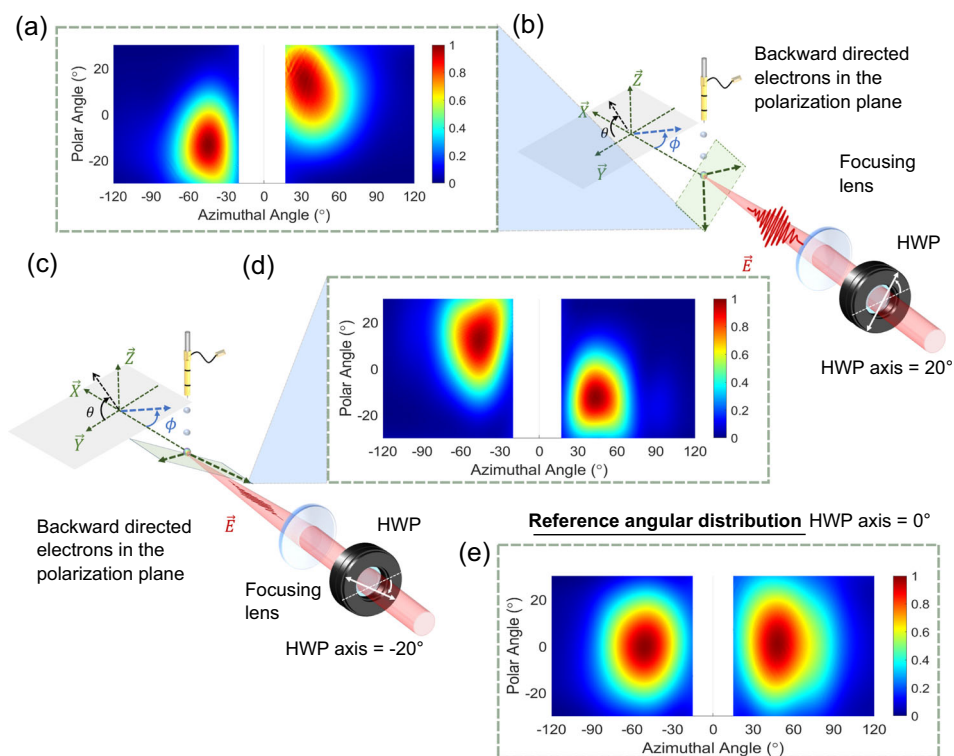
**Fig. 3 | Effect of pre-pulse on droplet target and subsequent electron generation.** **a** $T_{hot}$ dependence as a function of incident laser intensity, for electrons within 200 keV–1 MeV. Error bars (standard deviation) for each data point is calculated from the standard deviation of the calculated electron temperatures of three electron spectrograms, each acquired for a duration of 8 s. **b** Variation of electron emission angle as a function of laser intensity. The yields at 400 μJ and 700 μJ main pulse energy are multiplied by factors of 50 and 10 for clarity. **c** The effect of pre-pulse percentage on the X-ray yield. The corresponding pre-pulse energy in μJ is indicated on the top axis. The error (standard deviation) in signal lies within the diameter of the representative symbols. **d** Schematic of the shadowgraphy set-up imaging the effect of pre-pulse on the droplet. **e** Transverse shadowgraphy image of the droplets acquired at 2.6 ns after the pre-pulse interaction. **f** First drop shows the shadow of typical droplet without the pre-pulse irradiation. The red dotted curve indicates the cup-like structure.

the scattered light from the first pulse. The delay between the two pulses is varied using a delay stage to capture the target modifications caused by the pre-pulse as a function of time. The schematic of the set-up is presented in Fig. 3d. Droplets without the pre-pulse are also captured for reference in the same frame. The shadowgraphy image acquired at a delay of 2.6 ns shows the formation of hollow cup/cone-like concave structure at the front of the expanding droplet (Fig. 3e–f); More images are in the supplement, Supplementary Fig. 6). A video sequence (of images) is appended as Supplementary Movie 1.

**Numerical modeling**
As is evident from the experiments, the hot electrons are generated by the interplay of the pre-pulse and the main pulse effects on the target droplet. Initially, the pre-pulse leads to a hydrodynamic evolution of the droplet over 4 ns, followed by the main pulse interaction resulting in rapid electron generation. Therefore, to investigate and identify the underlying acceleration mechanism, a 2D hydrodynamic simulations followed by 2D particle-in-cell (PIC) simulations are performed. The 2D lagrangian radiation-hydrodynamics simulations are performed using the commercial code h2d with an ideal gas equation of state, an average-atom LTE ionization model, and a multi-group diffusion approximation for thermal radiation. These simulations are run with initial laser and target parameters identical to the collinearly propagating pre-pulse in the system. Conforming to the

experimental pre-pulse and main pulse delay, the simulations are run for 4 ns after the arrival of the pre-pulse, at which point a snapshot of the mass density of the mesh is taken. As expected, the hydrodynamic simulations also reveal the formation of a concave cup-like structure is also observed in the experiments. Figure 4a shows the mass density distortion, acquired from h2d simulations, 4 ns after the pre-pulse interaction. The position of the original droplet is shown by a white dotted semi-circle while the position of line-out profiles is demarcated by the white dashed lines. Besides, target deformation, a plasma gradient is also seen to be generated by the pre-pulse (Supplementary Fig. 7). Further details of the pre-pulse generated modifications are presented in Supplementary Note 5. Having extracted the modified target geometry and the plasma parameters from the h2d simulations, 2D PIC simulations are done to explore modifications in the main laser-plasma interaction process.

The main pulse interaction with the pre-pulse modified droplet is studied using two PIC codes: SMILEI[34] and EPOCH[35]. Typically, a simulation box size of $100 \times 100\lambda_0^2$ is divided into $3000 \times 3000$ cells, where the droplet is placed at the center. The droplet is modeled as a pre-ionized plasma represented by 49 macro-particles per cell. Ions are treated as a stationary background. The laser pulse is modeled by a Gaussian transverse profile with a waist radius of $W_0 = 12\lambda_0$ and a pulse-width of 24.3 fs. A virtual circular detector/screen surrounding the target is used to record the energy and angular distribution of the ejected electrons. Details of both the

**Fig. 4 | Numerical modeling of laser-droplet interaction. a** h2d radiation-hydrodynamic simulation shows a concave surface formed 4 ns after the pre-pulse interaction. **b** Comparison of the electron energy spectrum obtained from EPOCH 2D particle-in-cell (PIC) (blue dots) on the modified droplet geometry shown in the inset, at $8.5 \times 10^{16}$ W cm$^{-2}$ with experimentally obtained electron spectrum on LANEX at $4 \times 10^{16}$ W cm$^{-2}$ (black solid line). The yellow dots show electron energy spectrum obtained from EPOCH 2D PIC at $4 \times 10^{16}$ W cm$^{-2}$. The temperature fits for both these simulated spectra are shown in Supplementary Fig. 2. **c** Directed electron emission as observed in 2D EPOCH simulations. The laser is incident along the $x$ axis (white solid arrow) with its polarization along $y$ axis (white dashed arrows). **d** Electron spectrum obtained with 2D PIC EPOCH simulations with the plasma length scales of $L = 4\lambda$ and $L = 8\lambda$, where $\lambda = 800$ nm. A two-temperature component of the spectrum with $L = 8\lambda$ (in agreement with the h2d simulations) show both the 200 keV and 1 MeV temperature components.
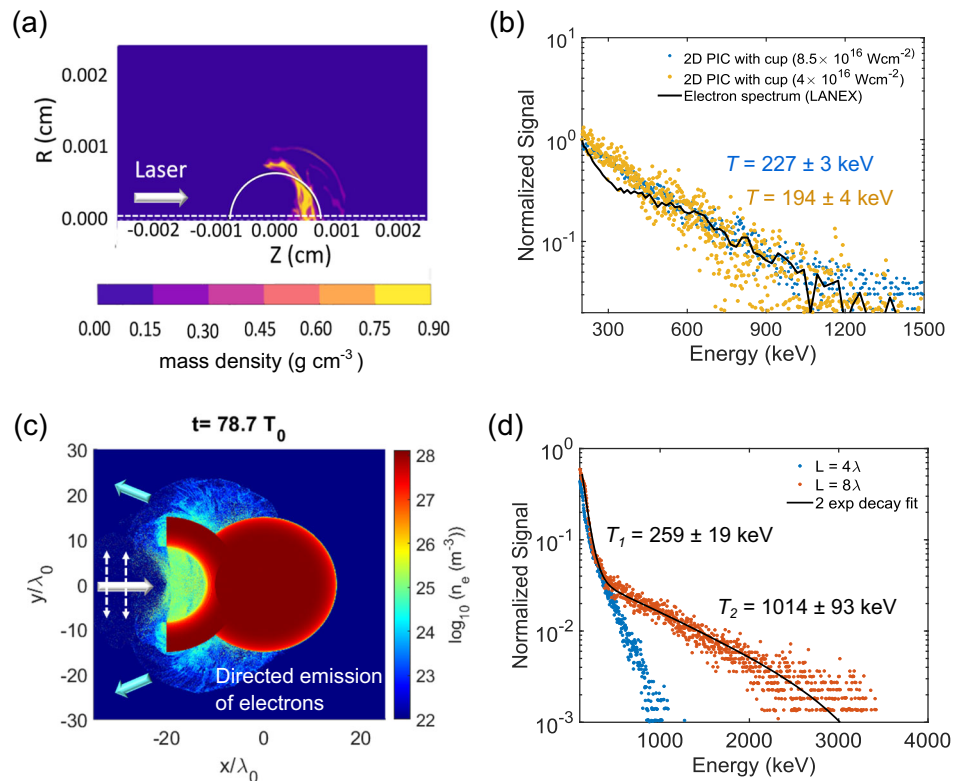


2D hydrodynamic and the 2D PIC simulation are provided in the Methods section. The simulations are carried out in 2D rather than 3D due to the limitations in computational resources. We note that there could consequently be an overestimate of the hot electron temperature and flux in the simulations[42,43]. The major reason for this potential discrepancy is the neglect of the loss of laser energy through laser-plasma interaction processes, such as SRS, in directions perpendicular to the polarization plane. However, the simulations performed here are not intended to achieve a precise quantitative match to the experimental results, but rather to identify the key electron generation mechanisms in the system. From simulations of several shapes and the plasma gradients (see Supplementary Fig. 8) we decipher the optimal conditions responsible for the hot electron generation. We find that a cup-shaped structure with overdense walls filled in with a plasma having a preferential density gradient is optimal for comparing with the spherical drop scenario for the same laser parameters. A dramatic rise in the electron temperature from ~11 keV (spherical undistorted target Fig. 1b) to 227 keV (Fig. 4b data with $8.5 \times 10^{16}$ W cm$^{-2}$) and 259 keV ($T_1$ component of Fig. 4d) along with the characteristic directed emission (Fig. 4c) are observed. Further, from PIC we find that for the optimum scale length of $8\lambda$ (similar to the h2d calculations), where $\lambda = 800$ nm, the 1 MeV component is significantly enhanced, resulting in a maximum hot electron temperature of $1014 \pm 93$ keV ($T_2$ component of Fig. 4d).

## Discussion

The compelling correlation with the experimental spectrum in the 200 keV-1 MeV region, shown in Fig. 4b and the electron angular distribution, shown in Fig. 4(c), validates the decisive roles played by the plasma-filled cup in the electron. From a one-to-one correlation, presented below, of the experimental and simulation results with the prevalent properties of parametric instabilities, we identify TPD to be the dominant acceleration mechanism.

i) In TPD, the presence of a pre-plasma gradient with a long scale-length enhances the non-linear growth of the generated plasmons, following which a plasmon decay releases high energy electrons. This necessity of a long scale-length pre-plasma for hot electron generation, is also revealed in both numerical (Supplementary Fig. 8b) and experimental (Fig. 3c,

Supplementary Fig. 9 and Supplementary Note 6) studies of the laser-droplet interaction.

ii) The symmetry of the systems allows the generation of directed plasmons along the $45^o$ direction on either sides of the laser propagation axis[20,44]. This is also revealed from a spatio-temporal analysis of the electric fields from the PIC simulation results, in and about the droplet cavitation surface. Supplementary Fig. 10, Supplementary Movie 2a and Fig. 5a show, how the hot electrons are ejected in the optimized case(cup-hs3) by presenting the electron density evolution at a few selected instants. It is seen that upon initial hitting by the incident laser, plasma waves are formed in the non-uniform plasma inside the cup. These waves propagate towards the droplet boundary and eventually crash on the high density region, followed by the release of a copious amount of electrons. These electrons originate from the edges of the hemispherical cavitation structure and the droplet base and are beamed in the backward direction at large angles. These features are present only when the modified pre-plasma conditions are included, thus initiating oblique-incidence TPD. The forward moving plasma waves are shown to impinge on the cup boundary releasing hot electrons (Supplementary Fig. 10 and Supplementary Movie 2a). In comparison, due to the absence of a critical density barrier, the backward directed plasma waves are shown to grow unhindered resulting in resonant excitation of electrons to relativistic energies. This is also evident from the temporal evolution of the electron momentum components shown in Supplementary Figs. 11 and 12. Supplementary Fig. 11 shows the temporal snapshots of electron momentum ($\mathbf{p}_x$) as a function of propagation distance $\mathbf{x}$. The laser, incident from the left boundary of the simulation box is shown to excite the electrons resonantly. Inset shows the region of interest(white rectangle) considered for tracking the particle momentum as a function of time. On further propagation, the optical pulse is reflected from the overdense cup-structure (Supplementary Movie 2b, snapshots presented in Supplementary Fig. 13). A similar process takes place in the y direction, as depicted in Supplementary Fig. 12. The reflected pulse in this situation is also seen to enhance the plasma wave amplitude. Supplementary Movies 3a, b and 4a, b show the temporal evolution of the momentum and the electric field simultaneously to observe the above discussed process. Further details are presented in
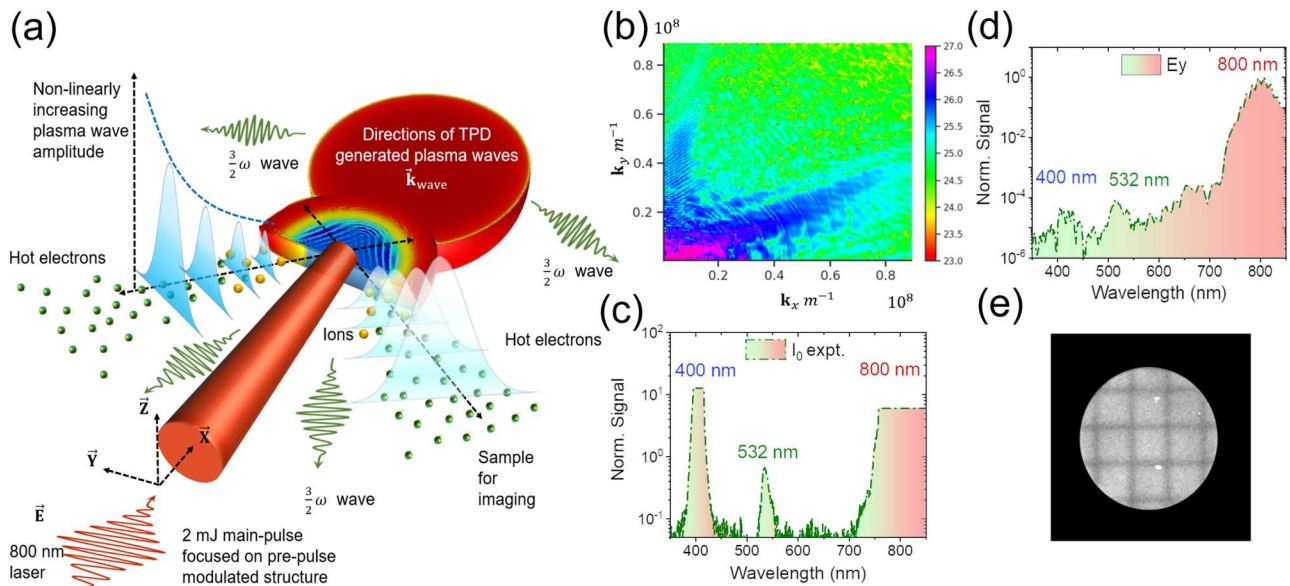
**Fig. 5 | Signatures of two-plasmon decay (TPD) accelerated electrons and their application. a** Schematic of hot electron generation mechanism in the pre-pulse modified droplet. The incident laser-pulse decays via TPD in the pre-plasma gradient of the cup at $n_{cr}/4$ (quarter-critical plasma density). The plasmons generated (marked with black dashed arrows) resonantly oscillate the electrons in the plasma. As they are damped, the accelerated electrons are ejected as backward-directed jets, along with 3/2 harmonic emission. **b** 2D **k**-space spectrum of the plasma fields in the cavitation region (demarcated by the white box in Supplementary Fig. 11 (inset)) shows generation of directed plasma waves with wave vectors capable of generating the observed relativistic electrons. **c** The experimentally measured optical spectrum along the backward-propagation direction (opp. to normal incidence). $I_0$ denotes the normalized incident intensity on the spectrometer. **e** Fourier spectrum of the electric field components obtained along the backward-propagation direction. As the 3/2 harmonic light propagates primarily along the negative $-x$ axis in this region, the 532 nm peak is distinct in the $\mathbf{E}_y$ component as opposed to the $\mathbf{E}_x$ component of the wavelength spectrum. **e** The backward directed electrons at ±50° can be used for electron radiography. This is demonstrated with an electron image of a 41 μm thick Ni wire grid acquired with a 100 ms LANEX exposure.

supplementary Notes 7 and 8. It is seen that while the electrons gain energy by wave breaking in the **x** direction, damping of the plasma waves releases hot electrons in the **y** direction. For accelerating electrons by this mechanism to a sub-relativistic (200 keV) and a relativistic temperature component, plasma waves with wave vector **k** of magnitudes $4.5 \times 10^6$ m$^{-1}$ and $5.64 \times 10^6$ m$^{-1}$, respectively, are required. Fourier analysis of the plasma wave dispersion at the apex of the cup (Fig. 5b), reveal wave vectors with the appropriate magnitudes to be maximized along the ±45° and ±135° directions in the laser polarization plane. PIC simulations show that the stronger 200 keV component can be seen even when the plasma scale length is small ($L = 4\lambda$, Fig. 4d). Increasing the plasma scale length to $8\lambda$, as estimated by the hydrodynamic simulations, clearly shows the appearance of the relativistic temperature component corroborating with the experimental results.

iii) However, in conventional targets, TPD, is unable to substantially enhance electron temperatures with near-threshold, ultrashort pulses. We overcome this difficulty by generating the cup-shaped dynamic structure. TPD is known to be stronger for oblique incidence[29–31], where the instability interacts with longer effective pre-plasma length scales as opposed to normal incidence. The cup geometry significantly lowers the TPD enhancement threshold by ensuring oblique-angle incidence. This also explains the varying electron emission angle with increasing laser intensity (Fig. 3b). At low intensities ($8 \times 10^{15}$ W cm$^{-2}$), the absence of a strong critical density concave surface initiates TPD only at high incidence angles and electrons are emitted dominantly at ± 90°. Increasing the laser intensity, progressively drives 'perpendicular' TPD at the back of the cup, changing the emission angle to ± 45° for $4 \times 10^{16}$ W cm$^{-2}$.

iv) In addition, angular distribution of the electron emission, shown in Fig. 4c from the 2D PIC are in good agreement with the obtained experimental electron angular distribution, shown in Fig. 2e.

v) The TPD induced plasma waves are expected to interact with the incident light and stimulate Raman scattering. The $\omega/2$ plasma wave coupling with the incident light at $\omega$ (800 nm) should generate 3/2 $\omega$ light at about 530 nm[33]. Figure 5c, d shows the 3/2 $\omega$ emission observed both in

experiment and simulations respectively, providing direct evidence of the TPD mechanism. Both the experimental and the numerical spectrum from the droplet, are captured along the back-reflected direction (opposite to the laser incidence). As the electric field component is always perpendicular to the direction of propagation, for backward-propagation only $\mathbf{E}_y$ component of 3/2 harmonic observed from the numerically calculated Fourier spectrum. While at the side of the target both $\mathbf{E}_x$ and $\mathbf{E}_y$ spectrum show the existence of 532 nm peak (Supplementary Fig. 3e, f).

vi) Lastly, as the two plasmons in TPD are generated in the plane of laser polarization, rotation of the incident laser polarization changes the electron emission plane. The synchronous rotation of the electron emission plane with the laser polarization, as observed in Fig. 2, provides the final verification for TPD as the dominant electron acceleration process. In typical long pulse experiments several parametric instabilities like SRS, TPD and Stimulated Brillouin Scattering (SBS) compete[43]. For short-pulse (≤100 fs) laser-matter interaction, ion motion can be neglected[45]. However, in such experiments with steep plasma gradients(<10 μm), both TPD and SRS can concomitantly exist in the near quarter-critical density leading to a hybrid mode of acceleration and the generation of 3/2 $\omega$ emission[46]. TPD is favored in the current experiment, not only due to lower intensity threshold[22], but also as a consequence of the oblique-angle of incidence within the cavity[29–31]. This is also inferred from the experimentally observed direction of electron emission. However, the interplay of TPD and SRS, is highly dependent on parameters like laser intensity, pre-plasma parameters, focal spot size and the like[46] and quantitative statements regarding the same require further investigation of observables like the angular distribution of 3/2 $\omega$ emission[45].

Aside from the key result of enhancing the electron temperature by 2-3 orders of magnitude, we demonstrate the suitability of such size-limited droplet targets for producing high-flux, directional electron beams for radiographic applications. Figure 5e shows a well-resolved lens-less transmission image of a 41 μm thick Ni wire grid, generated by electrons on a LANEX scintillation screen with a 100 ms exposure time.

## Conclusions

In conclusion, we present here a dynamic, laser-controlled, target structuring scheme for achieving relativistic electron temperatures, over a few-micron acceleration length at $4 \times 10^{16}$ W cm$^{-2}$, only. The experimental results show that this laser-plasma optimization technique generates two beams of electrons, having 200 keV and 1 MeV electron temperature components with the maximum electron energy extending beyond 4 MeV with mJ/pulse 25 fs lasers. A summary of the entire mechanism (with the actual plasma wave profiles from the 2D PIC simulations) is illustrated in Fig. 5a. First, the spherical droplet interaction with the pre-pulse creates a concave surface and a low-density plasma front-surface. The concave geometry and the pre-plasma gradient, optimizes the growth of instabilities during the main pulse interaction, following which wave damping or wave-breaking ejects the observed, relativistic electrons. The scheme very well explains why: (a) the generation of hot electrons requires the presence of both cavitation and a plasma density gradient in the cup, (b) the electrons are emitted at $\pm50^0$ with respect to the incident laser direction in the plane of polarization (c) the angle of dominant electron emission changes with the laser intensity, from $90^0$ at the intensity threshold to $30$-$60^0$ at higher intensities. The simulations verify this TPD driven electron generation mechanism and explain the dependencies of the electron properties with the laser parameters. These results, therefore, demonstrate a simple yet elegant mechanism of accelerating electrons way beyond the ponderomotive limit, leading to highly efficient hot electron production even at modest intensities.

Looking to the future, we expand upon two important points regarding the suitability of this scheme for applications. Firstly, our droplet source operates at 1 MHz and is synchronized with the 1 kHz laser. This has enabled us to acquire electron radiographs even with few laser pulses. There are consequently no apparent barriers to synchronization with a higher repetition rate system, with a resultant increase in the average current. Secondly, as the electrons are directed by the laser-plasma transient fields, the electron emission is also expected to be ultrashort (few tens of fs) in nature, as seen in the simulation. Combining these two features would result in ultrashort electron pulses having both high peak brightness and high average flux. This would be invaluable for applications like radiography and diffraction. The laser system used in these experiments has an active pointing stabilization system assuring high-pointing stability. As the droplets are synchronized with the laser pulses with a delay generator, the shot-to-shot drift of the laser-droplet synchronization is negligible. We infer this from the 14 µm and 41 µm resolution of electron and X-ray radiographs, respectively, acquired for $\sim10^5$ shots. Of course there is a slow long-term drift in the laser-droplet alignment (primarily in the vertical direction), which can be corrected by changing the timing in the delay-generator and also automated by the implementation of a feed-back loop. However, these drifts occur over long-time scales (>30 mins) and do not limit the electron spectrum measurement or the high-resolution radiography applications, the data for which is acquired within periods of a few seconds. It is important to keep in mind that the droplet is also a hard X-ray source with energies extending from few keV to 200 keV, emitted directly from the droplet, capable of acquiring X-ray images in a few seconds. Similar to the electrons these X-rays are also expected to be pulsed[47–49], making them ideal spectroscopic probes for studying ultra-fast chemical dynamics[50]. The demonstration of such an electron acceleration mechanism with its myriad applications in a low energy, moderate-intensity regime, therefore opens an exciting and new direction for the development of genuinely compact table-top accelerators that can be driven by readily available low cost, high-repetition rate, femtosecond lasers.

## Methods

### Electron, X-ray and optical measurements

The electron energy measurements are performed using an ESM with LANEX and Image plates (IP) as electron detectors. The droplet generated electrons are collimated with a 2 mm aperture before entering the ESM. A magnet of strength 0.11 T is used to bend these electrons onto the detector, the position of incidence being proportional to the electron energy.

The LANEX is used for online detection of the incident electrons within the range of 200 keV–1 MeV. Integrated counts over 8 s exposure are collected using an 8-bit CCD, with a 540 nm bandpass filter to collect the light generated from the LANEX scintillation only. For high energy trace collection, beyond 1 MeV, longer acquisition is performed using BAS-MS IP detectors. To prevent a reduction in IP signal by ambient light, a 10 µm Al foil is wrapped around the IP detector. The IPs are read using GE's Amersham Typhoon image scanner. The signal strength $N(\mathbf{x})$ measured as a function of the splat position, $\mathbf{x}$, on the detector is converted to $N(E)$ vs $E$ using position-to-energy calibration calculated using the experimentally measured magnetic profile and ESM geometry based on the standard position to energy conversion formulation[51]. The calibration curves are presented in the supplement Supplementary Fig. 14 and Supplementary Note 9. The final electron spectra obtained from LANEX and IP are corrected for the LANEX sensitivity values[52] and the PSL sensitivity and fading time characteristics, respectively, obtained from literature[53,54]. The spectrally resolved signals are fitted to a Maxwellian distribution (functional form is exp(-E/kT)), similar to the previous methodology used for temperature determination from electron spectrum[55], where $E$ is the energy of the electron, $k$ is the Boltzmann constant, and $T$ is the hot electron temperature.

To corroborate the electron energy measurements, bremsstrahlung X-ray measurements are also performed. X-rays generated from the experiment are acquired using both a MINIPIX detector (for measurement of X-rays up to 300 keV) and a NaI(Tl) detector (100 keV to 6 MeV) coupled to a multi-channel analyser (MCA) in the pulse counting mode, where each photon incident on the crystal coupled to a PMT, gives a signal proportionate to the energy of the photon. The NaI(Tl) detector is triggered and gated to acquire a signal only during the main pulse incidence. To avoid pile-up in spectroscopic measurements for the high-energy X-rays, a 6 mm Pb filter is used. This demands an acquisition time of about 900 s to generate a background subtracted X-ray spectrum up to 6 MeV(Supplementary Fig. 3). Calibration of the MINIPIX detector is performed using L$\alpha$ and L$\beta$ lines of Pb having energies of ~10 keV and ~12 keV, respectively. While for the NaI(Tl) detector is carried out using $^{137}$Cs, $^{22}$Na and $^{133}$Ba radioactive gamma sources. The filter transmission corrections are accounted for in the reported spectrum[56]. The signal collected for a number of pulses is used to generate a histogram that gives the number of photons of a given energy impinging on the crystal. This energy spectrum is again fitted to the Maxwell-Boltzmann distribution to derive the temperature.

In addition to the electron energy, the spatial profile of the emitted electrons is also captured with electron angular distribution measurements. IPs spanning from 0° to 360° in the azimuthal ($x$–$y$) plane and $-40°$ to 40° in the polar(z) plane are placed at a distance of 3.2 cm around the droplet target. The IP geometry in the Cartesian coordinate is illustrated in Supplementary Fig. 3c, where (0,0,0) indicates the target droplet position. Each IP is wrapped with 110 µm Al foil to prevent both optical light and low energy electrons from being incident on the detector. Circular openings are made both in the entry and exit direction for unhindered propagation of the laser beam. Further details are presented in Supplementary Note 10 and in Supplementary Fig. 15. Each angular distribution measurements are acquired for an exposure of 30 s. Electron spectra for emission directions of 45° and 90° for different angles of laser polarization are also shown in Supplementary Fig. 16 and explained in Supplementary Note 11.

The optical spectrum of the laser-plasma emission is measured along the back-reflected direction using a spectrometer. The supercontinuum background is captured by misaligning the laser from the droplet. The TPD optical spectrum is obtained for the optimal alignment of the laser and droplet, monitored by the maximization of the electron energy on the LANEX. Figure 5c shows the supercontinuum subtracted optical spectrum as obtained from the experiments.

### Discussion on the shadowgraphy imaging of the droplet target modified by the pre-pulse

In order to observe the effect of the pre-pulse on the target structure, shadowgraphy imaging is set up. The schematic of the set-up is shown in

Fig. 3d. The principle of the measurement, in brief, is as follows: the main laser pulse is split into two beams P1 and P2. The first beam P1 containing 8% of the beam energy, and the second P2 contains the rest 92%. The beam P1 is incident first on the drop target and acts as the pre-pulse, the beam P2 then arrives at a given time delay perpendicular to P1 to image the structural change of drop due to pre-pulse. P2 is converted to 400 nm wavelength using a BBO crystal. Since the X-ray yield varies marginally with pre-pulse variation from 4 to 10% (Fig. 3c), we have chosen an 8% pre-pulse for our shadowgraphy experiments. The delay between P1 and P2 has been varied from 2.6 ns to 6 ns, and a CCD, time-synchronized with P2, is used to capture the droplet images as P2 arrives. A few snapshots of the droplet structure at 2.6 ns are shown in Fig. 3e, f. Similar structures are also observed at later time scales. However, the shadowgraphy images do not reveal any information about the target parameters like temperature or density. For such information, we take the help of the 2D hydrocode-h2d. Also, in the main experiments, the pump-probe delay is about 4 ns and the pre-pulse intensity ~5%. The shadowgraphy parameters though similar to this, are not exactly identical. We, therefore, use the hydrocode using the exact experimental parameters to find the structural modification and the associated plasma parameters of the hydrodynamically modified target.

In addition to the target deformation, the hydrodynamic simulations also show an extended region of low-density gas/plasma existing in front of the drop target (Supplementary Fig. 7), which is shown to be essential for the generation of relativistic electrons.

## 2D hydrodynamic simulations

The 2D lagrangian radiation-hydrodynamics simulations are performed using the code h2d. h2d is a commercial product of Cascade Applied Sciences email larsen@casinc.com. The spherical target is simulated with an initial radius of 7.5 µm and an initial density of 0.792 g cm$^{-3}$. The laser pulse having an 800 nm wavelength, 0.1 mJ energy, 25 fs FWHM is simulated with a sech$^2$ temporal profile and a Gaussian spatial profile with an 11 µm FWHM. A ray-tracing algorithm brought the energy to the target, mimicking a focusing optic employed in the experiment. The final on-target intensity is $0.2 \times 10^{16}$ W cm$^{-2}$, 5% that of the main pulse. The simulations are run for 4 ns after the arrival of the pulse, at which point a snapshot of the mass density of the mesh is taken. The underdense plasma length scale of $8.6 \pm 0.1$ µm is obtained from an exponential fit $\mathbf{n}(\mathbf{Z}) = n0\,exp(-\mathbf{Z}/L)$[55] of Supplementary Fig. 7b, where $\mathbf{n}(\mathbf{Z})$ is the electron density profile along the line cut $\mathbf{R} = 0$, $\mathbf{Z}$ is the direction of laser propagation with $\mathbf{Z} = 0$ being the drop surface prior to pre-pulse interaction, n0 is the electron density at $\mathbf{Z} = 0$ after 4 ns of the pre-pulse interaction and $L$ is the plasma length scale.

## 2D Particle-in-cell simulations

The 2D PIC simulations are performed using two codes SMILEI[34] and EPOCH[35]. For the simple spherical droplet discussed earlier (Supplementary Fig. 8a nocup), the plasma electron density is initialized at $\mathbf{n}_e/n_c = 10$ for $\mathbf{r}\ /\lambda_0 < 5$ and $n_e/n_c = 10\cos(\pi(\mathbf{r} - 5)/10)$ for $5 < \mathbf{r}/\lambda_0 < 10$, where $\mathbf{r} = \sqrt{(x-50)^2 + (y-50)^2}$ is the radius measured to the center of the droplet at $\mathbf{x} = 50\lambda_0$ and $\mathbf{y} = 50\lambda_0$. For the cup-like pre-plasma (Supplementary Fig. 8a cup-hs3), the droplet electron density is given by $\mathbf{n}_e/n_c = 7$ for $\mathbf{r}/\lambda_0 < 10$ and $\mathbf{r}_c/\lambda_0 > 13$, and $\mathbf{n}_e/n_c = 7\cos(\pi(\mathbf{r} - 10)/10)$ for $\mathbf{r}/\lambda_0 < 15$ and $\mathbf{r}_c/\lambda_0 > 13$, where $\mathbf{r}_c = \sqrt{(x-30)^2 + (y-50)^2}$ is the radius measured to the cup center at $\mathbf{x} = 30\lambda_0$ and $\mathbf{y} = 50\lambda_0$; the cup electron density is given by $\mathbf{n}_e/n_c = 7\exp(-(13 - \mathbf{r}_c)^2/4) + 0.01$ for $\mathbf{x}/\lambda_0 > 30$ and $\mathbf{r}_c/\lambda_0 < 13$. A laser of normalized vector potential $\mathbf{a} = a_0 \sin(\pi t/\tau)^2$ is launched from the left boundary, where $a_0 = 0.2$ and $\tau = 25T_0 = 25\lambda_0/c$ correspond to a peak intensity of $8.56 \times 10^{16}$ W cm$^{-2}$ and a pulse duration of 24.3 fs (FWHM in intensity profile), respectively. The laser parameters in EPOCH simulation are kept identical to the SMILEI simulation. In addition, in the EPOCH simulations, an ionization module is included by the addition of a background of Ar (has similar ionization energy to $N$) neutral atoms, represented by 49 macro-particles per cell in the simulations corresponding to a gas density of $10^{17}$ cm$^{-3}$. Both simulations provide similar results as shown in

Fig. 4b, d. Further, we observe with the EPOCH simulations that a plasma length-scale of $8\,\lambda$ is optimum for producing hot electrons up to 3.5 MeV.

## Data availability
The datasets that are presented in the manuscript are available from the corresponding author upon reasonable request.

## Code availability
MATLAB codes used for the analysis of the datasets are available from the corresponding author upon reasonable request.

## References
1. Faure, J. et al. A laser-plasma accelerator producing monoenergetic electron beams. *Nature* **431**, 541–544 (2004).
2. Geddes, C. G. R. et al. High-quality electron beams from a laser wakefield accelerator using plasma-channel guiding. *Nature* **431**, 538–541 (2004).
3. Mangles, S. P. D. et al. Monoenergetic beams of relativistic electrons from intense laser-plasma interactions. *Nature* **431**, 535–538 (2004).
4. Lundh, O. et al. Few femtosecond, few kiloampere electron bunch produced by a laser-plasma accelerator. *Nat. Phys.* **7**, 219–222 (2011).
5. Kneip, S. et al. Bright spatially coherent synchrotron X-rays from a table-top source. *Nat. Phys.* **6**, 980–983 (2010).
6. Wilks, S. C. et al. Absorption of ultra-intense laser pulses. *Phys. Rev. Lett.* **69**, 1383 (1992).
7. Kluge, T. et al. Electron temperature scaling in laser interaction with solids. *Phys. Rev. Lett.* **107**, 205003 (2011).
8. Tajima, T. & Dawson, J. M. Laser electron accelerator. *Phys. Rev. Lett.* **43**, 267 (1979).
9. Malka, V. Plasma wake accelerators: introduction and historical overview. CERN Yellow Report CERN-2016-001, **1** (2016).
10. He, Z.-H. et al. High repetition-rate wakefield electron source generated by few-millijoule,30 fs laser pulses on a density downramp. *N. J. Phys.* **13**, 053016 (2013).
11. Salehi, F. et al. MeV electron acceleration at 1 kHz with <10 mJ laser pulses. *Opt. Lett.* **42**, 215–218 (2017).
12. Rajeev, P. P. et al. Metal nanoplasmas as bright sources of hard X-ray pulses. *Phys. Rev. Lett.* **90**, 115002 (2003).
13. Zigler, A. et al. Enhanced proton acceleration by an ultrashort laser interaction with structured dynamic plasma targets. *Phys. Rev. Lett.* **110**, 215004 (2013).
14. Bagchi, S. et al. Hot ion generation from nanostructured surfaces under intense femtosecond laser irradiation. *Appl. Phys. Lett.* **90**, 141502 (2007).
15. Krishnamurthy, M. et al. A bright point source of ultrashort hard x-ray pulses using biological cells. *Opt. Exp.* **20**, 5754 (2012).
16. Sarkar, D. et al. Silicon nanowire based high brightness, pulsed relativistic electron source. *APL Photonics* **2**, 066105 (2017).
17. Anand, M. et al. Hot electrons produced from long scale-length laser-produced droplet plasmas. *Laser Phys.* **17**, 408–414 (2007).
18. Feister, S. et al. Relativistic electron acceleration by mJ-class kHz lasers normally incident on liquid targets. *Opt. Express* **25**, 18736 (2017).
19. Vallières, S. et al. Enhanced laser-driven proton acceleration using nanowire targets. *Sci. Rep.* **11**, 2226 (2021).
20. Ebrahim, N. A. et al. Hot electron generation by the two-plasmon decay instability in the laser-plasma interaction at 10.6 µm. *Phys. Rev. Lett.* **45**, 1179 (1980).
21. Figueroa, H. et al. Stimulated Raman scattering, two-plasmon decay, and hot electron generation from underdense plasmas at 0.35 µm. *Phys. Fluids* **27**, 1887 (1984).

22. Boyd, T. J. M. The trouble with laser-plasma interactions. *Plasma Phys. Control. Fusion* **28**, 1887 (1986).

23. Singh, P. K. et al. Two-plasmon-decay induced fast electrons in intense femtosecond laser-solid interactions. *Phys. Plasmas* **27**, 083105 (2020).

24. Cole, J. M. et al. Laser-wakefield accelerators as hard x-ray sources for 3D medical imaging of human bone. *Sci. Rep.* **5**, 13244 (2015).

25. Cole, J. M. et al. High-resolution $\mu$CT of a mouse embryo using a compact laser-driven X-ray betatron source. *PNAS* **115**, 6335–6340 (2018).

26. Maier, A. R. et al. Water-window X-ray pulses from a laser-plasma driven undulator. *Sci. Rep.* **10**, 5634 (2020).

27. Nunes, J. P. F. et al. Liquid-phase mega-electron-volt ultrafast electron diffraction. *Struct. Dyn.* **7**, 024301 (2020).

28. Hazra, D. et al. Electron radiography with different beam parameters using laser plasma accelerator. *Phys. Rev. Accel. Beams* **22**, 074701 (2019).

29. Schuss, J. J. Absolute two plasmon parametric decay of obliquely incident electromagnetic waves in an inhomogeneous plasma. *Phys. Fluids* **20**, 1121 (1977).

30. Wen, H. et al. Two-plasmon decay instability in inhomogeneous plasmas at oblique laser incidence. *Phys. Plasmas* **23**, 092713 (2016).

31. Seka, W. et al. Experimental investigation of the two-plasmon-decay instability at oblique incidence. *APS Div. Plasma Phys. Meet. Abstr.* **45**, FO2.001 (2003).

32. Baffigi, F. et al. X-ray conversion of ultra-short laser pulses on a solid sample: role of electron waves excited in the pre-plasma. *Phys. Plasmas* **21**, 072108 (2014).

33. Wen, H. et al. Dynamics of laser-produced plasmas through time-resolved observations of the $2\omega_0$ and $3/2\omega_0$ harmonic light emissions. *Phys. Rev. Lett.* **37**, 95 (1976).

34. Derouillat, J. et al. SMILEI: a collaborative, open-source, multi-purpose particle-in-cell code for plasma simulation. *arXiv*, https://arxiv.org/abs/1702.05128 (2018).

35. Arber, T. D. et al. Contemporary particle-in-cell approach to laser-plasma modelling. *Plasma Phys. Control. Fusion* **57**, 113001 (2015).

36. Bussolino, G. C. et al. Electron radiography using a table-top laser-cluster plasma accelerator. *J. Phys. D: Appl. Phys.* **46**, 245501 (2013).

37. Bulanov, S. V. et al. Oncological hadrontherapy with laser ion accelerators. *Phys. Lett. A* **299**, 240–247 (2002).

38. Malka, V. et al. Practicability of protontherapy using compact laser systems. *Med. Phys.* **31**, 1587–1592 (2004).

39. Li, Y. T. et al. Spatial distribution of high-energy electron emission from water plasmas produced by femtosecond laser pulses. *Phys. Rev. Lett.* **90**, 165002 (2003).

40. Wu, H. C. et al. A simple estimate of resonance absorption of femtosecond laser pulses by liquid droplets. *Appl. Phys. B* **77**, 687–689 (2003).

41. Shahzad, M. et al. Diagnosis of energy transport in iron buried layer targets using an extreme ultraviolet laser. *Phys. Plasmas* **22**, 023301 (2015).

42. Wen, H. et al. Three-dimensional particle-in-cell modeling of parametric instabilities near the quarter-critical density in plasmas. *Phys. Rev. E* **100**, 041201(R) (2019).

43. Gu, Y.-J. et al. Multi-dimensional kinetic simulations of laser radiation absorption and electron acceleration in inhomogeneous underdense plasma. *Nucl. Fusion* **61**, 066014 (2021).

44. Baumgärtel, K. Topics on nonlinear wave-plasma interaction (Birkhäuser, 1987).

45. Veisz, L. et al. Three-halves harmonic emission from femtosecond laser produced plasmas with steep density gradients. *Phys. Plasmas* **11**, 3311–3323 (2024).

46. Tsymbalov, I. et al. Hybrid stimulated Raman scattering-two-plasmon decay instability and 3/2 harmonic in steep-gradient femtosecond plasmas. *Phys. Rev. E* **102**, 063206 (2024).

47. Reich, C. et al. Yield optimization and time structure of femtosecond laser plasma $K\alpha$ sources. *Phys. Rev. Lett.* **84**, 4846–4849 (2000).

48. Zhavoronkov, N. et al. Generation of ultrashort $K\alpha$ radiation from quasipoint interaction area of femtosecond pulses with thin foils. *Appl. Phys. Lett.* **86**, 244107 (2005).

49. Zamponi, F. et al. Femtosecond hard X-ray plasma sources with a kilohertz repetition rate. *Appl. Phys. A* **96**, 51–58 (2009).

50. Chergui, M. & Zewail, A. H. Electron and X-ray methods of ultrafast structural dynamics: advances and applications. *ChemPhysChem* **10**, 28–43 (2009).

51. Kazuo, A. Tanaka calibration of imaging plate for high energy electron spectrometer. *Rev. Sci. Instrum.* **76**, 013507 (2005).

52. Wu, Y. C. et al. Note: absolute calibration of two DRZ phosphor screens using ultrashort electron bunch. *Rev. Sci. Instrum.* **83**, 026101 (2012).

53. Bonnet, T. et al. Response functions of imaging plates to photons, electrons and 4He particles. *Rev. Sci. Instrum.* **84**, 103510 (2013).

54. Zeil, K. et al. Absolute response of Fuji imaging plate detectors to picosecond-electron bunches. *Rev. Sci. Instrum.* **81**, 013307 (2010).

55. Culfa, O. et al. Plasma scale-length effects on electron energy spectra in high-irradiance laser plasmas. *Phys. Plasmas* **21**, 043106 (2014).

56. X-ray mass attenuation coefficients, https://www.nist.gov/pml/x-ray-mass-attenuation-coefficients (2004).

## Acknowledgements

## Author contributions

M.K. and A.M. conceived the idea of the laser-droplet experiments in consultation with R.G. and M.A.; A.M. conducted the droplet experiments with support from S.T., S.V.R., R.S., S.S., D.R., and R.Y.K. Supplementary experiments with the boric acid particles were conducted by R.Y.K. and D.R.; R.M.G.M.T and A.P.L.R guided the 2D- PIC simulations done by R.S.; F.L. and Z.S. did the initial 2D PIC simulations. W.T. and J.P. did the 2D radiation-hydrodynamics simulations. R.S. and J.J. did the preliminary simulations to investigate the focusing effects, and S.S. performed the low-density plasma calculations. The manuscript was written by A.M. and M.K. with the help of the other authors.

## Competing interests

The authors declare no competing interests.

## Additional information